



Pt/CeCrO_{2-x}: A multifunctional catalyst for tandem catalysis of lignocellulose hydro-liquefaction and Guerbet reaction

Weichao Chou^a, Pingping Lu^a, Bin Lou^{a,*}, Weizhen Li^b, Chongchong Wu^{c,*}, Peng Wu^b, Zhuowu Men^b, Dong Liu^{a,*}

^a School of Chemistry and Chemical Engineering, China University of Petroleum, Qingdao 266580, China

^b National Institute of Clean-and-Low-Carbon Energy, Beijing 102211, China

^c CNOOC Institute of Chemicals & Advanced Materials, Beijing 102200, China

ARTICLE INFO

Keywords:

Lignocellulose
Catalytic transfer hydrogenation
Ethanol dehydrogenation
Hydrodeoxygenation
Wettability

ABSTRACT

Catalytic transfer hydrogenation (CTH) of lignocellulose liquefaction using renewable ethanol presents a promising alternative to conventional hydrogenation techniques. However, the development of efficient and stable multifunctional catalysts remains a significant challenge. Herein, a Pt/Ce₉Cr₁O_{2-x} catalyst was developed to facilitate the CTH reactions and achieve nearly complete utilization of lignocellulose. Isotope labeling experiments were conducted to elucidate the mechanism of CTH. The introduction of Cr³⁺ increased the density of surface oxygen vacancies, consequently enhancing the hydrodeoxygenation ability and metal anchoring. The solid solution structure promotes the electrons transfer from Cr atoms to Pt atoms, forming electron-rich Pt^{δ+} species that promote ethanol dehydrogenation and lignocellulose hydrodeoxygenation. Furthermore, Pt/Ce₉Cr₁O_{2-x} catalyst provided optimal acid-base sites and hydroxyl groups, thereby improving ethanol upgrading efficiency and wettability.

1. Introduction

Biomass is an abundant and renewable energy resource that offers a sustainable and environmentally friendly alternative to fossil fuels for long-term industrial activities [1–4]. Therefore, it is imperative to develop efficient and selective strategies for the direct conversion of raw lignocellulose into liquid fuels and value-added chemicals. Various methods, including lignin-first strategies [5,6], pyrolysis [7,8], gasification [1,9], and hydro-liquefaction [10,11], have been utilized to obtain carbon resources in biomass. However, lignin-first strategies suffer from high organic solvent consumption, complicated reaction conditions, and poor net energy yield. In order to achieve a high selectivity of target products, multi-step reactions with varying reaction conditions are often necessary, which inevitably results in a protracted and costly process [6]. Meanwhile, the pyrolysis gasification strategy often needs high temperature and pressure, which can result in the emission of harmful gases such as CH₄, CO, and CO₂, etc [1]. Also, this strategy undoubtedly diminishes the production of valuable high carbon substrates and generates intractable coke. In contrast, the hydro-liquefaction process can efficiently convert lignocellulose into

liquid fuels and value-added chemicals in one step under mild conditions using a multifunctional catalyst. It has low operating temperature, high energy efficiency, and low tar yield compared to pyrolysis. Besides, this technique enables the direct utilization of wet biomass including seaweed and food residues, etc., eliminating the need of drying units and reduced the total production cost [12].

Due to the large amount of oxygen in biomass, it is crucial to remove excessive oxygen-containing functional groups [13]. Hence, multifunctional catalysts that possess excellent hydrodeoxygenation (HDO) capabilities are required to generate the desired products. Researchers have made significant efforts to explore heterogeneous catalysts, such as Cu-PMO [14], CdS QDs [15], Ni₂Al₃ alloy [1], and Pt/NbOPO₄ [16]. Nevertheless, these catalysts often face challenges such as high catalyst dosage, incomplete conversion, complex operation, and elevated hydrogen pressure that are frequently overlooked in laboratory-scale experiments. Furthermore, current studies on HDO often employ molecular hydrogen as the hydrogen donor, which usually requires high hydrogen pressure because of hydrogen's low solubility in the reaction medium [12,16,17]. The use of "gray" hydrogens not only increases infrastructure costs on an industrial scale but also poses significant

* Corresponding authors.

E-mail addresses: louloulove@163.com (B. Lou), chongchong.wu@ucalgary.ca (C. Wu), liudong@upc.edu.cn (D. Liu).

<https://doi.org/10.1016/j.apcatb.2023.123320>

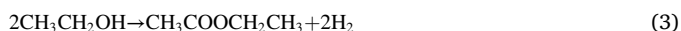
Received 25 July 2023; Received in revised form 18 September 2023; Accepted 21 September 2023

Available online 24 September 2023

0926-3373/© 2023 Elsevier B.V. All rights reserved.

safety risks, presenting an economic barrier to the sustainable development of the biomass upgrading industry [18]. To simplify the process, our current objective is to establish a catalytic system that is better suited for subsequent industrial-scale production. Additionally, we also aim to convert all components of raw biomass into advanced biofuels and chemicals in a single process while investigating alternative hydrogen donors. In order to better express the innovation of the current work, different catalytic systems reported for the total conversion of lignocellulose are summarized in Table 1.

To minimize reliance on external hydrogen, organic compounds like alcohols and formic acid can serve as hydrogen donors for substrate reduction during catalytic transfer hydrogenation [19,20]. Compared to acidic hydrogen donors, ethanol is neutral and non-corrosive, it is miscible with both water and bio-oil, and it has high hydrogen mass density and can be produced cheaply and renewably, which makes it an ideal hydrogen donor for large-scale applications [21,22]. However, there is a scarcity of reports concerning the utilization of ethanol dehydrogenation and the Guerbet reaction in biomass HDO. Nevertheless, there is scarcity of reports concerning the utilization of ethanol dehydrogenation and the Guerbet reaction in biomass HDO, often overlooking the hydrogen produced as a by-product [22]. An essential discovery in this field is Hensen's report, which demonstrates that employing ethanol as a capping agent, coupled with catalyzing Guerbet and esterification reactions, can effectively inhibit the formation of undesirable heavy by-products like chars [23]. This type of Guerbet reaction has been termed "borrowed hydrogen" chemistry. The reactions below indicate that the major products of ethanol upgrading are acetaldehyde, C₄₊ alcohols/esters, and hydrogen [4].



We previously investigated a one-step raw lignocellulose upgrading process in supercritical ethanol utilizing a Pt/CeCrO_{2-x} solid solution catalyst [10]. Remarkably, this process achieved nearly complete conversion of the material without the formation of coke, even without the use of external hydrogen. Doping CeO₂ with Cr³⁺ cations significantly increases the formation of oxygen vacancies and acid-base sites, resulting in catalysts with improved activity. Building on this foundation, we explored the "borrowed" hydrogen strategy for depolymerizing biomass via in-situ hydrogen transfer of ethanol dehydrogenation and the fundamental reasons for efficient mass transfer at the triphasic interface. This strategy can also reduce the catalyst under reaction conditions through in-situ hydrogen generation, which is an innovative

approach that has been rarely reported (Fig. 1).

Here, we follow up with our earlier work conducted on multifunctional Pt/CeCrO_{2-x} catalysts for biomass hydro-liquefaction. Specifically, we investigate the effect of catalysts with different Ce/Cr ratios on the physicochemical characteristics and structure-activity relationship by a wide number of techniques. Furthermore, we conducted deuterium isotope tracing experiments, along with GC-MS analysis and in-situ techniques to further investigate the hydrogen transfer mechanism. Our findings reveal that the Ce/Cr ratio can be used to tune the catalyst structure, surface hydroxyl group, acidity, and wettability, ultimately impacting its performance. Our results will identify the optimum catalyst for biomass transformation and enhance the feasibility and economics of industrial applications.

2. Experimental and methods

2.1. Chemicals and materials

The study utilized birch wood sourced from a local lumberyard in Qingdao, China. To ensure its purity, the material underwent multiple washes with deionized water. Afterward, the birch was dried at a temperature of 105 °C for 12 h. It was then ground to a particle size of approximately 250 μm to facilitate further analysis. The sawdust's detailed characteristics are listed in Table S1. Ammonia solution tetrahydrate (NH₃·H₂O, 25%–28%), anhydrous sodium sulfate (Na₂SO₄), ethanol, and ethanol-OD (>99.0%) were purchased from Sigma-Aldrich Industrial Corporation. Acetone, Ce(NO₃)₃·6H₂O, Cr(NO₃)₃·9H₂O, Pt(NO₃)₂ were obtained from Macklin. All chemical reagents were commercially supplied and used without additional purification.

2.2. Catalyst synthesis

The catalysts utilized in this study were synthesized by employing precipitation techniques, which were previously described by our research group. For instance, Pt/Ce₉Cr₁O_{2-x} catalyst was prepared in the following way: 11.72 g Ce(NO₃)₃·6H₂O and 1.21 g Cr(NO₃)₃·9H₂O, were dissolved in 100 mL of deionized water and stirred for 30 min. Aqueous ammonia solution was then added dropwise into the above solution with stirring vigorously at 60 °C until the precipitation was completed at pH = 10. The resulting yellow-brown slurry was centrifuged and washed with deionized water until the pH of the filtrate was neutral. The solid was dried at 110 °C overnight and then calcined at 500 °C for 4 h to obtain the Cr-doped CeO₂ support. 0.112 g of Pt(NO₃)₂ aqueous solution (approximately 2 wt%) was loaded onto the support by impregnation. Other catalysts with different Ce/Cr ratios were prepared using the same method as described above, and are named as Pt/CeO₂, Pt/Ce₉Cr₁O_{2-x}, Pt/Ce₇Cr₃O_{2-x}, Pt/Ce₅Cr₅O_{2-x}, Pt/Ce₃Cr₇O_{2-x}, and Pt/Cr₂O₃, respectively. Prior to the reaction, all catalysts were reduced in a tube furnace at 300 °C for 2 h in a gas mixture containing 10% H₂ and 90% N₂.

2.3. Catalytic tests and product analysis

The hydro-liquefaction of raw biomass and ethanol upgrading reactions were conducted in a 100 mL Teflon-lined stainless-steel autoclave. In a typical reaction, 20 g ethanol and 0.1 g catalyst were added. The reactor was purged with N₂ three times and then pressurized to an initial pressure of 2.0 MPa. The temperature was gradually raised to 300 °C under vigorous stirring and maintained at 300 °C for 5 h. Once the reaction was completed, the reactor was cooled down using cooling coils. The pressure variation of the autoclave was recorded during the reaction. The gaseous products were collected and analyzed by GC. The liquid/solid mixtures were separated by a pre-weighed filter paper and the reactor and residue were rinsed with acetone. The filtrate was dried over anhydrous sodium sulfate (Na₂SO₄) and then subjected to rotary evaporation until its weight was constant. The remaining products were

Table 1
The complete or direct valorization of lignocellulosic biomass.

| Feedstock | Catalyst | Reaction conditions | Products | Ref. |
|---------------|---|--|--|-----------|
| Birch | Pt/ Ce ₉ Cr ₁ O _{2-x} | 300 °C, 2 MPa N ₂ , 5 h, ethanol | Esters, High carbon ethanol, and monophenols | This work |
| beech | Ni ₂ Al ₃ alloy | 300 °C, 4 MPa H ₂ , 5 h, H ₂ O | Methane, C2-C4 natural gas, and carbon dioxide | [1] |
| Pine | Cu20-PMO | Step 1: 180 °C, 4 MPa H ₂ , 18 h, methanol; Step 2: 320 °C, 6 h, methanol | aromatic monomers, and aliphatic alcohols | [6] |
| Alkali lignin | Cu-Mg-Al Mixed Oxide Catalyst | 340 °C, 1 MPa N ₂ , 4 h, ethanol; | Esters, ethanol, and lignin monomers | [14] |
| Birch | Pt/NbOPO ₄ | 190 °C, 5 MPa H ₂ , 20 h, cyclohexane; | Pentanes, hexanes, and alkyl cyclohexanes | [16] |

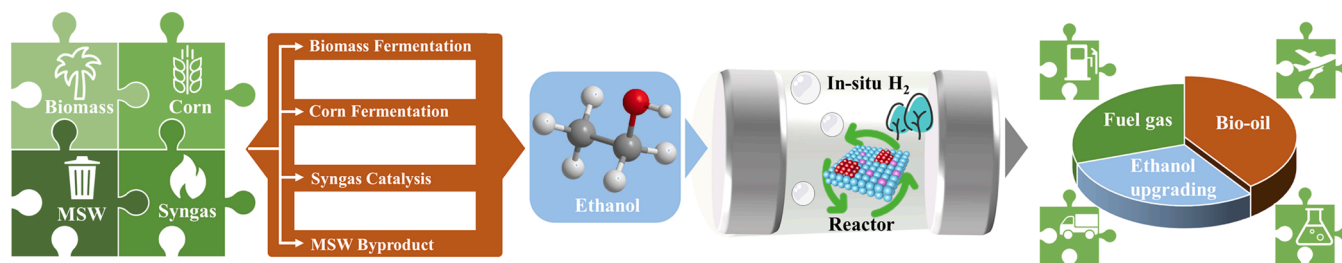


Fig. 1. Ethanol dehydrogenation is a crucial process for converting ethanol into valuable products and as a hydrogen source for biomass hydro-liquefaction. Ethanol's versatility, renewability, widespread availability, and low cost make it an attractive and cost-effective starting material for the Guerbet reaction.

classified as bio-oil and qualitatively analyzed by GC-MS equipped with a DB-5 column (30 m × 0.25 mm × 0.25 μm) and quantitatively analyzed by GC-flame ionization detector (FID). The injector temperature was kept at 300 °C. The oven temperature was programmed from 50 °C (hold 2 min) to 300 °C (hold 10 min) with a heating rate of 10 °C/min. Helium (99.999%) was used as the carrier gas with a constant column flow rate of 5 mL/min and a split ratio of 1:20. The recyclability of the Pt/CeCrO_{2-x} catalyst was investigated at 300 °C for 5 h using birch and ethanol as feedstock. After each reaction cycle, the spent samples were first separated from the liquid phase by filtration, then washed with acetone and dried at 100 °C overnight. Finally, the catalyst was reduced in a 10% H₂/90% N₂ flow at 300 °C for 2 h. To gain insight into the reaction mechanisms and hydrogen-transferred pathways, isotopic labeling experiments were conducted using deuterated n-butanol (CH₃CH₂OD) as a hydrogen source. After the reaction, the reaction mixtures were analyzed by GC-MS (Agilent 7890B-5977A). In the MS, the ion signals for *m/z* = 57 and 58 (base peak) was continuously monitored to determine the isotope content of the original gas sample. The product yield was calculated based on the equations below:

$$\text{Conversion (wt.\%)} = \left(\frac{\text{weight of initial lignocellulose (g)} - \text{weight of residual lignocellulose (g)}}{\text{weight of initial lignocellulose (g)}} \right) \times 100\% \quad (4)$$

$$\text{Yield of bio-oil (wt.\%)} = \left(\frac{\text{weight of bio-oil (g)}}{\text{weight of initial lignocellulose (g)}} \right) \times 100\% \quad (5)$$

$$\text{Yield of solid (wt.\%)} = \left(\frac{\text{weight of residue (g)} - \text{weight of catalyst (g)}}{\text{weight of initial lignocellulose (g)}} \right) \times 100\% \quad (6)$$

$$\text{Yield of gas (wt.\%)} = 100 - \text{Yield of bio-oil (wt.\%)} - \text{Yield of solid (wt.\%)} \quad (7)$$

2.4. Catalyst characterization

The X-ray diffraction (XRD, Bruker D8) was performed using a Cu-Kα radiation source at 40 kV.

The surface and pore properties of samples were measured by N₂ physisorption on Micromeritics ASAP 2020. All catalysts were degassed at 350 °C for 6 h before analysis.

X-ray photoelectron spectroscopy (XPS, Thermo ESCALAB250Xi) was performed to measure the composition and valence states of surface metals. Component fitting for each element was based on the Gaussian-Lorentzian product function with an 80% Lorentzian-Gaussian value using Shirley background.

Inductively coupled plasma-atomic emission spectrometry (ICP-AES,

VARIAN 720-ES) was conducted to obtain the Pt, Ce, and Cr metal content.

Electron paramagnetic resonance (EPR) spectroscopy measurement was performed on the instrument (Bruker EMXplus, Germany).

Raman spectra were measured on the instrument (InVia Reflex, Renishaw, England) with an excitation laser of 532 nm.

The oxygen storage capacity (OSC) measurements were carried out by the oxygen pulse injection method. Before analysis, the catalyst was reduced by H₂/He at 400 °C.

Electrochemical impedance spectroscopy (EIS) Nyquist spectrum was done using a CH Instruments, Inc. CHI660E electrochemical workstation. A standard triple electrodes cell was employed. 0.2 M Na₂SO₄ aqueous solution was employed as an electrolyte solution.

The high-resolution transmission electron microscope (HR-TEM, Tecnai F20) was used to investigate the morphology of the materials at a voltage of 200 kV.

High-angle annular dark-field scanning transmission electron microscopy (HAADF-STEM) images, energy dispersive X-ray (EDX) mapping scan were recorded on the Tecnai G2F20 STwin.

The chemical temperature-programmed desorption/reduction (TPD/TPR) properties of the catalyst surface were tested on the Micromeritics AutoChem II 2920 instrument.

In-situ Nicolet 6700 spectrometer equipped with a cell was used to record the Pyridine Fourier transform infrared spectroscopy (FT-IR) spectrum. The *in-situ* FTIR spectra of catalysts were collected through a Nicolet NEXUS470 FTIR spectrometer equipped with a cell. The samples were pressed into a self-supporting plate (8 mg, 13 mm diameter), and placed in an IR cell.

Thermogravimetric analysis (TGA) was carried out to analyze the carbon deposition of the spent catalyst under N₂ (Q500 V20.13 Build 39, TA Instrument).

Zeta potential was done by using a Malvern Instruments Ltd. Nano ZS90 Zetasizer. Ethanol was employed as solvent to imitate the actual working conditions of catalysts in the measurement.

Atomic Force Microscope (AFM) imaging was performed under a tapping mode feedback at 220 kHz using a Nanoscope Multimode 8 (Bruker, Santa Barbara) equipped with a 120 μm piezoelectric scanner.

3. Results and discussion

3.1. Characterization of Pt/CeCrO_{2-x} catalyst

The XRD patterns and textural properties of the prepared materials are presented in Fig. 2. The crystalline phase composition of the

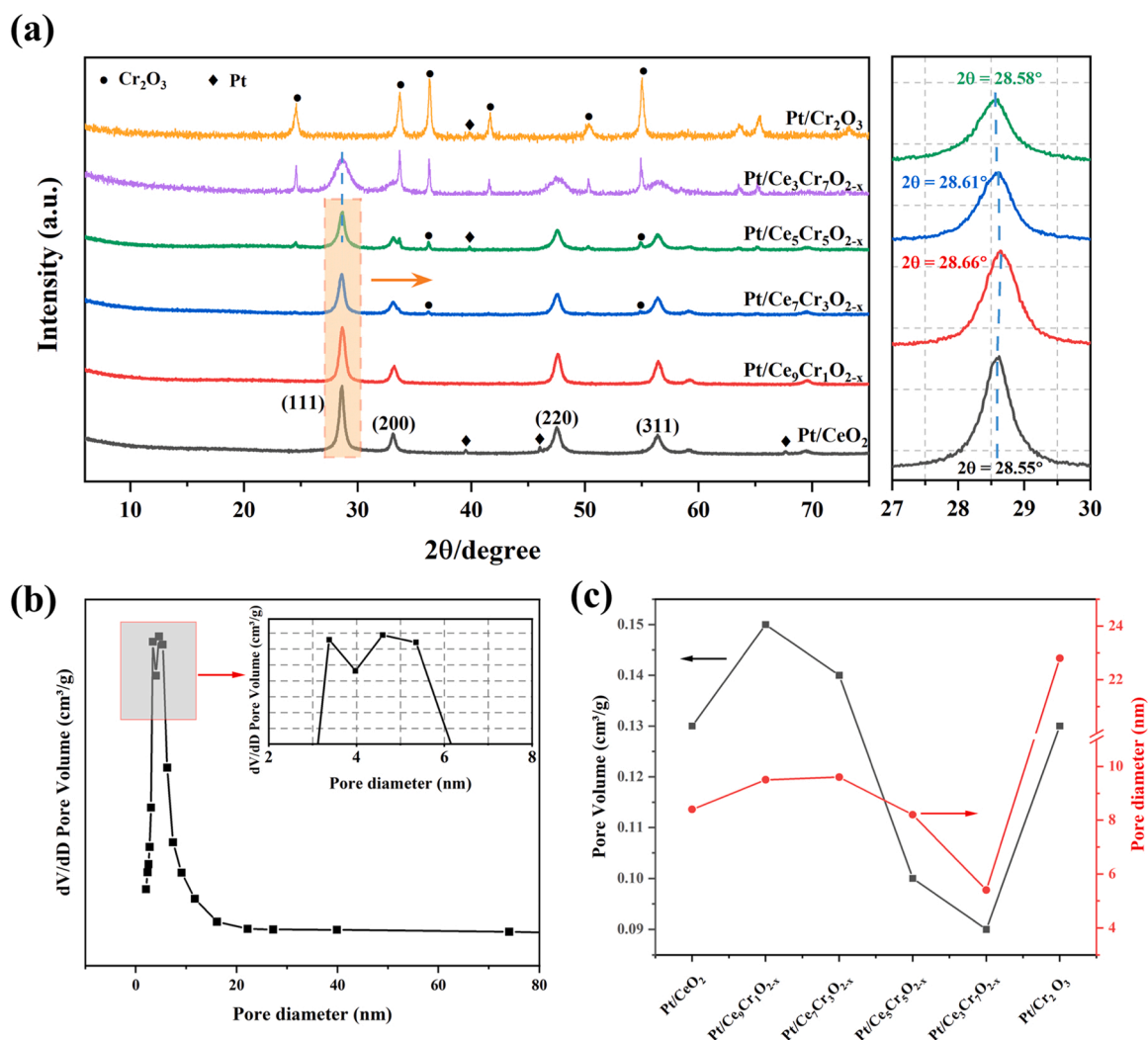


Fig. 2. (a) XRD patterns and partially enlarged profile of Pt/CeCrO_{2-x} catalyst with different Ce/Cr molar ratios. (b) Pore size distribution of Pt/Ce₅Cr₅O_{2-x}. (c) Relationship between the doping amount of Cr and the texture structure of the catalyst.

resulting composite oxide is determined by the Ce/Cr ratio. For the Pt/CeO₂ catalyst in Fig. 2a, the three strongest peaks were observed at 2θ of 28.6°, 47.5°, and 56.3°, corresponding to diffraction of the (111), (220), and (311) facets, respectively, according to JCPDS No. 34-0394 [10]. It is noteworthy that three small diffraction peaks were detected at 39.5°, 46.0°, and 67.1°, corresponding to the Pt nanoparticles. However, after modifying the sample with a certain amount of Cr, the aforementioned diffraction peaks disappeared, indicating that the introduction of Cr³⁺, whose valence state was confirmed by XPS below, dissolved into the CeO₂ and hindered the crystallization of surface Pt.

The coordination numbers and ionic radii of Ce⁴⁺ and Cr³⁺ ions play a crucial role in the structure and properties of mixed metal oxide. The incorporation of Cr³⁺ into the CeO₂ lattice to form a solid solution structure leads to a slight lattice shrinkage, which increases the 2θ value of the strongest (111) peak [24]. This transformation may be concerned with the lattice strain caused by the presence of Cr³⁺ (0.62 Å) ions became too large for the Ce⁴⁺ (0.87 Å) lattice to accommodate at the same coordination number [25]. However, as the content of Cr continued to increase and exceeded a critical value (Pt/Ce₅Cr₅O_{2-x}), the solid solution structure fails to regenerate and instead transforms into mixed metal oxides (CeO₂ and Cr₂O₃), resulting in the peak reverted back to lower 2θ value.

The N₂ adsorption-desorption isotherms and corresponding pore size distributions are presented in Fig. S1 and Table S2. All the samples

exhibited a type IV isotherm along with an H₃-type hysteresis loop, indicating the presence of irregular mesopores in the catalyst structure [26]. The pore size distribution of Pt/Ce₅Cr₅O_{2-x} and Pt/Ce₃Cr₇O_{2-x} exhibits two peaks, further suggesting the existence of two metal oxides in the support (Figs. 2b and S1e). The doping of Cr³⁺ significantly affected the growth of the catalyst lattice during precipitation and modified the cell parameters of the catalyst (Table S2). As illustrated in Fig. 2c, the pore size and volume initially experienced a slight increase with the increase of Cr content, followed by a considerable decrease. However, the pore size of the Pt/Cr₂O₃ catalyst is significantly larger than other catalysts, indicating that the Ce/Cr ratio can control the texture structure of the catalyst.

As depicted in Fig. 3, the particle size and morphology of the catalysts can also be controlled by adjusting the volume of Cr. The addition of Cr preserves the spherical shape of CeO₂ particles while increasing its content leads to a reduction in particle size. This decrease is particularly pronounced when the solid solution structure is disrupted (9.45–7.18–5.67 nm). Compared to Pt/CeO₂, Pt/Ce₉Cr₁O_{2-x}, +Pt/Ce₇Cr₃O_{2-x}, Pt/Ce₅Cr₅O_{2-x} and Pt/Ce₃Cr₇O_{2-x} exhibit significantly smaller the particle sizes. This reduction can be attributed to the inhibitory effects of excessive Cr on nucleation and growth of CeO₂. The addition of Cr altered the surface free energy and tension of the catalysts, which consequently impacted the catalyst's interface [27].

High-angle annular dark-field scanning transmission electron

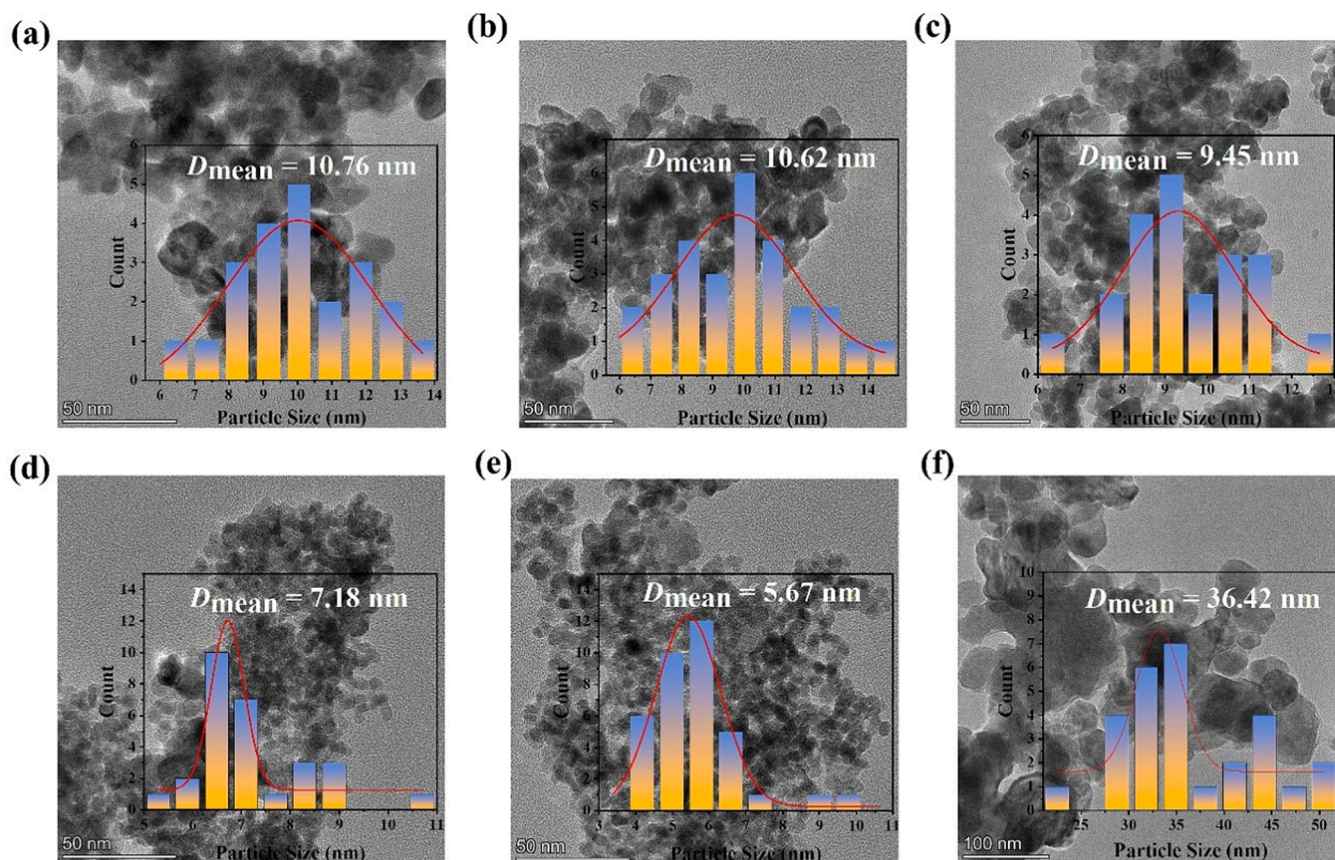


Fig. 3. TEM images and average particle size of (a) Pt/CeO₂, (b) Pt/Ce₉Cr₁O_{2-x}, (c) Pt/Ce₇Cr₃O_{2-x}, (d) Pt/Ce₅Cr₅O_{2-x}, (e) Pt/Ce₃Cr₇O_{2-x}, (f) Pt/Cr₂O₃.

microscopy (HAADF-STEM) and energy dispersive X-ray spectroscopy (EDS) mapping were conducted to analyze the distribution of the elements, as depicted in Fig. 4. For Pt/CeO₂ catalysts, the metal tends to be agglomerated at the edges of the CeO₂. For Cr-modified catalysts, the Pt, Cr, and Ce elements are distributed uniformly. Notably, when the Cr doping level reaches the threshold of solid solution structure disruption, Pt particles once again aggregate at the periphery of the support. Fig. S2 presents the high-resolution HR-TEM and EDS mapping images of the Pt/Ce₅Cr₅O_{2-x} catalyst. The images showed typical features of Cr₂O₃ (110) faces ($d=0.248$ nm) [28]. This result provides additional evidence supporting the promotion effect of the Ce-Cr solid solution structure on Pt dispersion.

3.2. Direct hydrodeoxygenation of raw woody biomass

The catalysts with various Ce/Cr ratios were evaluated using birch sawdust as the feedstock. Fig. 5a illustrates the solid and liquid yields obtained from the catalysts. The results indicate that Pt supported catalysts exhibit significantly higher activity than CeO₂ alone. This suggests that Pt is the active site of the HDO reaction. Subsequently, the addition of trace amounts of Cr further decreased the solid yield, which proved to be an extremely effective strategy for enhancing overall carbon utilization. The decrease in solid phase yield is accompanied by the increase in gas phase yield, with relatively little change in liquid-phase yield. Typical gas phase components are listed in Table S3. The presence of Pt and Cr resulted in higher amounts of CO, CO₂, and C₂ alkane and olefin products, indicating that the Pt/Ce₉Cr₁O_{2-x} catalyst exhibits improved decarbonylation and ethanol dehydrogenation capabilities, leading to increased H₂ production.

The information depicted in Fig. 5b reveals a substantial reduction in the yield of oxygenated products, accompanied by an impressive 96% conversion of raw lignocellulose. This can be attributed to the significant

production of H₂ (42.8 mmol) from ethanol dehydrogenation reaction (Table S3). In contrast, CeO₂ and CeCrO_{2-x} only produced trace amounts of hydrogen. Due to the complex composition of feedstocks, the hydro-liquefaction process of lignocellulose is highly intricate and typically results in the generation of numerous products. The main components of typical Pt/Ce₉Cr₁O_{2-x} in the liquid phase production are provided in Table S4. In this paper, we demonstrate the direct catalytic conversion of raw woody biomass into two groups of chemicals with remarkable yields. Through the utilization of our catalytic strategy, not only the carbohydrate fraction, i.e., cellulose and hemicellulose, were selectively converted to alcohol or diols with excellent yields up to 40.3%, but also the conversion of the lignin component into mono-phenols with a yield of 19.1% (based on the liquid phase). The main products comprise ethyl acetate, furan, 2, 3-dihydro, pentanone, 1-butanol, 3-pentanol, cyclohexanol, phenol and phenol, 4-methyl, etc. The product categories can be observed in Fig. 5b, where the Pt/Ce₉Cr₁O_{2-x} catalyst exhibits the most favorable HDO performance. The relative abundance of oxygen-containing products such as acids, aldehydes/ketones, and esters were significantly reduced, while the content of higher carbon alcohols exhibited a substantial increase. Moreover, we observed a high content of *n*-butanol and ethyl acetate in the product resulting from the dehydrogenation of ethanol, as well as the aldol condensation of the dehydrogenation product acetaldehyde (Eqs. (1)–(3)). The entire reaction encompasses dehydrogenation and hydrogenation processes, where the disparity in hydrogenation can be transferred to the lignocellulosic hydro-liquefaction reaction, which will be discussed in detail below.

To evaluate the recyclability of the top-performing catalyst, Pt/Ce₉Cr₁O_{2-x}, was subjected to the same reaction conditions for five cycles. According to Fig. 6, the catalytic performance of the catalyst gradually declined with increasing cycles, and significant deactivation was observed by the fifth cycle. After the reaction, ICP-AES analysis was

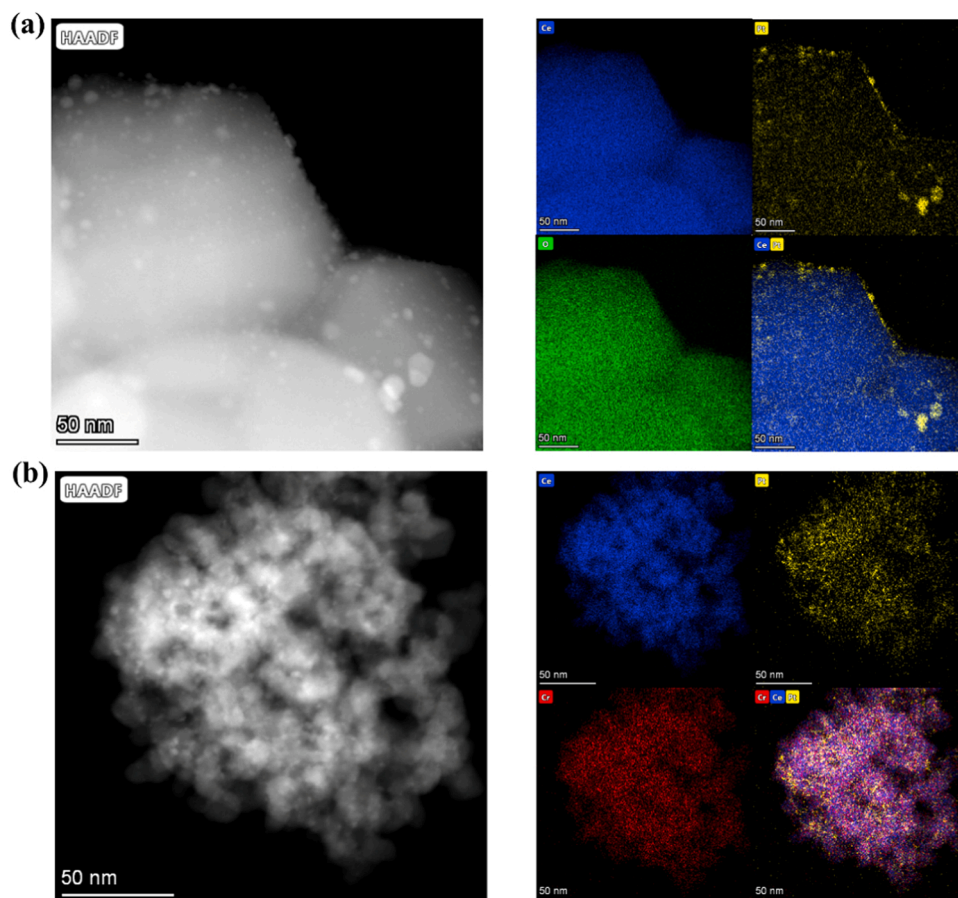


Fig. 4. HAADF-STEM and mapping images of (a) Pt/CeO₂, (b) Pt/Ce₉Cr₁O_{2-x}.

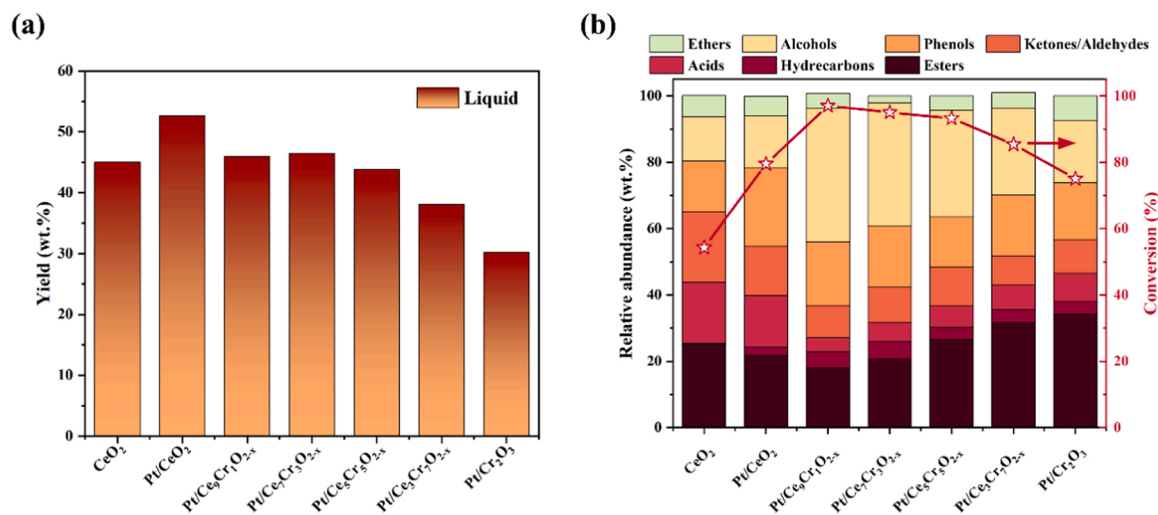


Fig. 5. Catalytic performance of catalysts for the hydro-liquefaction of lignocellulose. (a) The mass yield of the liquid phase. (b) Conversion and product distribution. Reaction conditions: 300 °C, 2 MPa N₂, 1 g feedstock, 0.2 g catalyst, 20 g ethanol.

conducted (Table S5). The results revealed that some metal leaching and catalyst mass loss occurred under long-term harsh reaction conditions. XPS analysis revealed that the leached Cr was present in trivalent chromium form rather than hexavalent chromium, which helps reduce environmental pollution (Fig. S3). TGA analysis demonstrated that the used catalyst contained a substantial amount of deposited coke, identified as low-order-degree graphite carbon, with a mass yield of 9.83 wt% at approximately 420 °C (Fig. 6b). The accumulation of coke on the

catalyst surface can obstruct the active sites, leading to catalyst deactivation. As shown in Fig. 6c and d, the distribution of Ce and Cr remained uniform, but the Pt particles exhibited slight agglomeration from 1.28 nm to 1.45 nm. Therefore, the observed catalyst deactivation during the cycle test could be attributed to the combined effects of metal species leaching, Pt agglomeration, and coke accumulation.

Catalytic transfer hydrogenation (CTH) is a technique that employs ethanol as a hydrogen donor and is also known as "borrowing hydrogen"

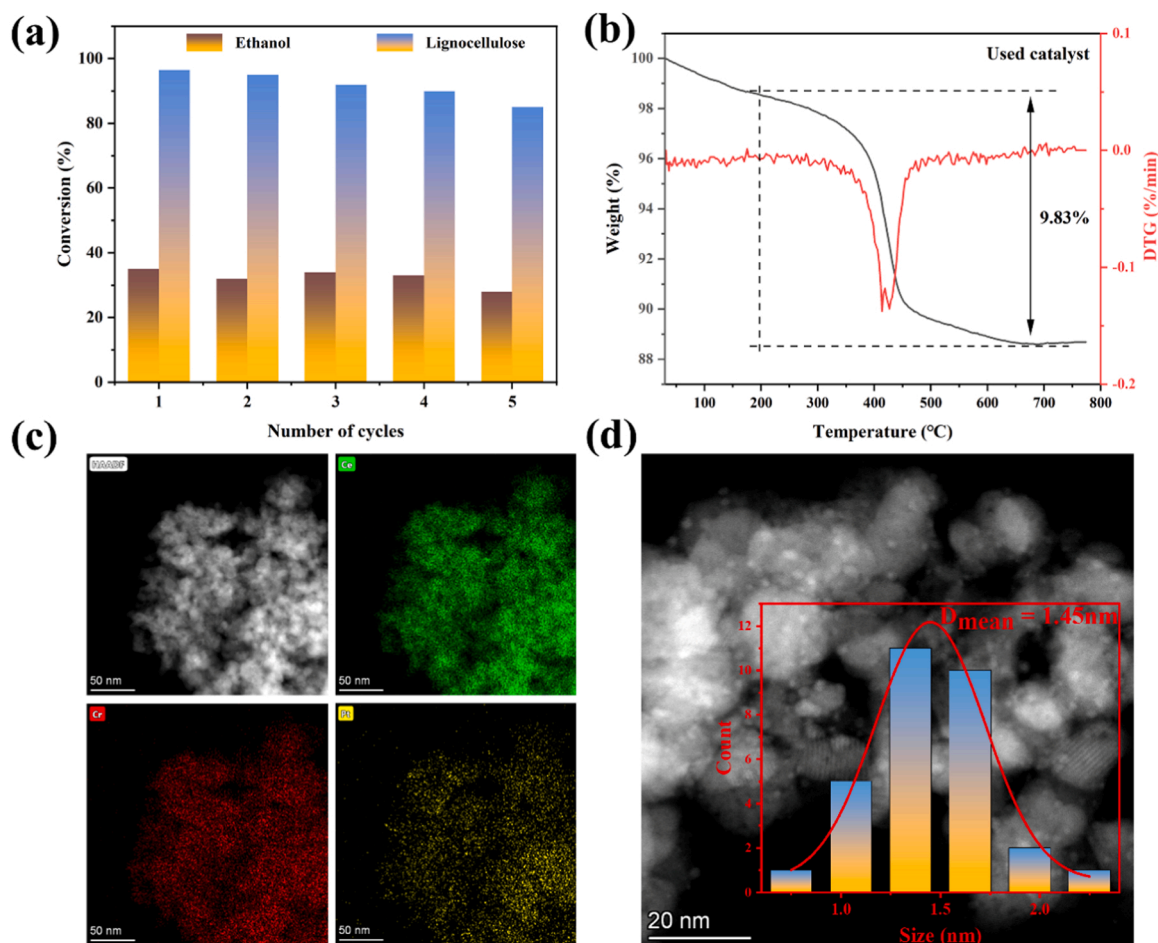


Fig. 6. The stability test of Pt/Ce₉Cr₁O_{2-x} catalyst. (a) Recycling performance of ethanol grading and hydro-liquefaction. (b) TGA and DTG curve. (c) EDS mapping images of used catalyst. (d) HAADF-STEM images and average particle size of Pt.

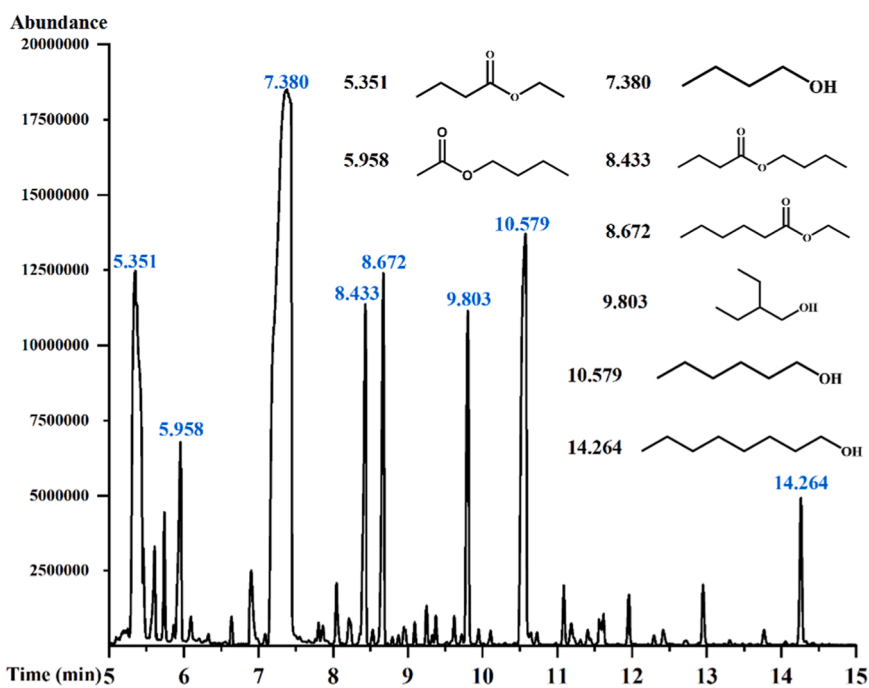


Fig. 7. Typical GC-MS spectra of the ethanol Guerbet reaction. Reaction conditions: 300 °C, 2 MPa N₂, 0.2 g Pt/Ce₉Cr₁O_{2-x} catalyst, 20 g ethanol.

chemistry [29,30]. Instead of directly supplying hydrogen, this method transfers it from ethanol to the substrate via multifunctional catalysts. Previous studies on lignocellulose hydro-liquefaction have frequently utilized high initial hydrogen pressure [16,31,32]. To overcome this challenge, a new process has been developed using catalytic ethanol via the Guerbet reaction to generate the necessary reducing equivalents in the form of H radicals [23]. In this work, the dehydrogenation reaction of ethanol is the main source of hydrogen production, generating acetaldehyde and ethyl acetate. The Typical GC-MS spectra of the Guerbet reaction was shown in Fig. 7. Ethyl acetate is a notable ester that can be industrially produced through ethanol dehydrogenation, and the process also yields reclaimable hydrogen. This method of generating endogenous hydrogen has rarely been applied in the biomass field and the relevant research has not received sufficient attention.

To elucidate the individual contributions of hydrogen and ethanol, we separately examined the effect of exogenous hydrogen on the Guerbet reaction. Details on these experiments and conclusions are provided in the Supplementary Note S1. It was found that the presence of a hydrogen atmosphere had no positive effect on the conversion of ethanol dehydrogenation. Due to the high activity of the ethanol dehydrogenation reaction, excess hydrogen can be used to reduce the catalyst (Fig. S5). To validate our speculation, we utilized deuterated ethanol-OD as a hydrogen source to gain more insight into the reaction mechanism using Pt/Ce₉Cr₁O_{2-x} catalysts. The GC-MS fragmentation in Figs. 8 and S6 demonstrated that the deuterated butanol produced by ethanol upgrading has a molecular weight of 1 amu and 2 amu greater than that of C₄H₉OH [33,34]. This parent ion increased indicating that the H atom in ethanol products was replaced by a deuterium (D) atom. This suggests that active H generated in situ acts as the hydrogen donor and is used for the hydrogenation of crotonaldehyde [35]. To further eliminate the impact of active H on the catalyst surface, we performed an H₂-TPD experiment. Fig. S7 shows that the hydrogen storage capacity of Pt/Ce₉Cr₁O_{2-x} is 2.3 times higher than that of Pt/CeO₂, as calculated by peak area. These results confirm that the addition of Cr can enhance the H₂ adsorption, activation, and spillover effect of the catalyst, which is consistent with the catalytic performances of the two catalysts [36].

3.3. Catalyst wettability and acidity

Catalysts with improved wettability can promote the adsorption and transfer of reactants and products, and further enhance the catalytic activity [37]. Our experimental results demonstrate that the Cr doped catalysts exhibit significantly higher dispersion in ethanol than other catalysts as shown in Fig. S8. Notably, the Pt/Ce₉Cr₁O_{2-x} catalyst

displayed no discernible stratification in ethanol solvent, even when subjected to the same static settling time as the other catalysts. This suggests that the Pt/Ce₉Cr₁O_{2-x} catalyst possesses superior stability and wettability in ethanol. To further demonstrate the wettability of the catalysts, we measured the ethanol droplet contact angles. As can be seen in Fig. 9a, the Pt/CeO₂ surface was highly hydrophobic, with a contact angle of 132°. In contrast, the hydrophilicity of the other surfaces generally increased with the increase of Cr content from 132° to 21°. To evaluate the surface oxophilicity or nucleophilicity, the zeta potential was measured to analyze the concentration of surface adsorbed oxygen species. During zeta potential measurements, the samples were suspended in deionized water in very low concentrations to make sure that the pH of each system remained constant [38]. As depicted in Fig. 9b, we can see that the zeta potential of the Pt/Ce₉Cr₁O_{2-x} catalyst changed to negative values after the addition of Cr, implying the abundance of negative adsorbed oxygen species. The strong nucleophilic nature of the catalyst surface indicates that the catalyst can provide a large number of electrons when the reactants adsorb and dissociate. This is crucial for the activation of either ethanol or hydrogen. Zeta potentials and contact angle measurements indicate that the functionalized catalysts are more hydrophilic and negatively charged than the Pt/CeO₂.

Defect chemistry is widely recognized as a crucial factor in determining the electronic structure, ionic conductivity, and catalytic activity of metal oxides [39]. Electrochemical impedance experiments were conducted to investigate the impact of Cr doping on the electronic environment of the catalysts (Fig. 9c). The results showed that the charge transfer within the CeCrO_{2-x} support is more favorable than that of the pure CeO₂ catalyst, providing further evidence that defects induced by lattice strain can impact the electron state and ionic conductivity [40]. Electron paramagnetic resonance spectra of the Cr-doped supports show a higher presence of intrinsic defects. These defects contribute to the hydrophilic nature of the samples, which is advantageous for heterogeneous catalysis (Fig. 9d).

Furthermore, surface hydrophilicity is closely related to the morphology and the number of polar groups [41,42]. Fig. 9(e and f) display the 3D atomic force microscopy (AFM) images of the Pt/CeO₂ and Cr-modified catalysts, and Fig. S9 shows the AFM micrographs of other catalysts. The root means square roughness (R_q) was calculated to evaluate the surface roughness. The surface of the Pt/CeO₂ catalyst (R_q = 0.310 μm) sample is fairly flatter than the Pt/Ce₉Cr₁O_{2-x} (R_q = 0.437 μm). According to the Wenzel and Cassie-Baxter models, a rougher surface would be more hydrophilic for hydrophilic catalysts as it provides a greater surface area for solvent adhesion [43]. Conversely, a rougher surface will be more hydrophobic for a hydrophobic catalyst, as it provides more surface area for air to adhere to, resulting in a composite solid-liquid-air triphasic interface. Hence, for hydrophilic Pt/Ce₉Cr₁O_{2-x} catalysts, a certain amount of Cr would increase the catalyst surface roughness, thereby improving catalyst wettability. Besides, we employed in-situ FT-IR, and XPS O 1 s to investigate the difference in the surface hydroxyl group between these catalysts. Fig. 9(g and h) shows the FT-IR spectra of the prepared samples. The peaks at 3600 and 1300 cm⁻¹ can be ascribed to the stretching and bending vibration of hydroxyl groups [44,45]. We found that the Pt/Ce₉Cr₁O_{2-x} catalyst has a significantly higher peak intensity for the IR adsorption ascribed to hydroxyl groups compared to the other catalysts. This indicates that Pt/Ce₉Cr₁O_{2-x} has the highest concentration of surface hydroxyl groups. Hydroxyl groups can form hydrogen bonds with alcohols, which is beneficial for the dispersibility in the autoclave and hydrophilic ability of the catalyst. Furthermore, the XPS techniques were executed to clarify the surface oxygen species of catalysts (Fig. S10). The O 1 s spectra indicated that the peak centered at ca. 532.1 eV can be attributed to a mixture of surface hydroxyl functional groups [10,43]. According to the peak area, it was observed that the modification of Cr significantly increased the concentration of hydroxyl groups on the catalyst's surface. The EPR results suggest that the Pt/CeCrO_{2-x} catalysts offer more intrinsic defects, thus leading to the

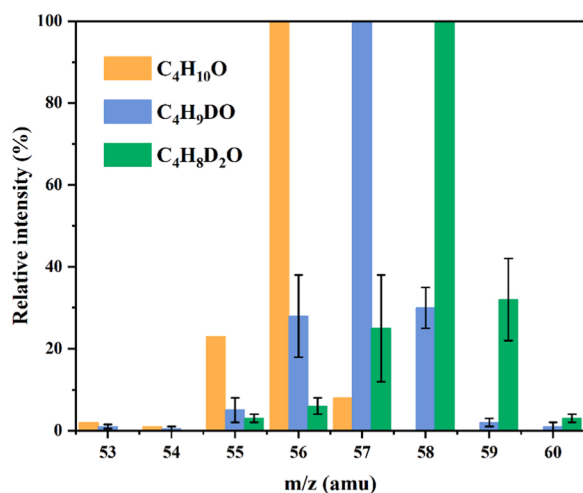


Fig. 8. Mass spectrum of butanol obtained from ethanol-OD under Pt/Ce₉Cr₁O_{2-x}. (reaction conditions: 300 °C, 5 h).

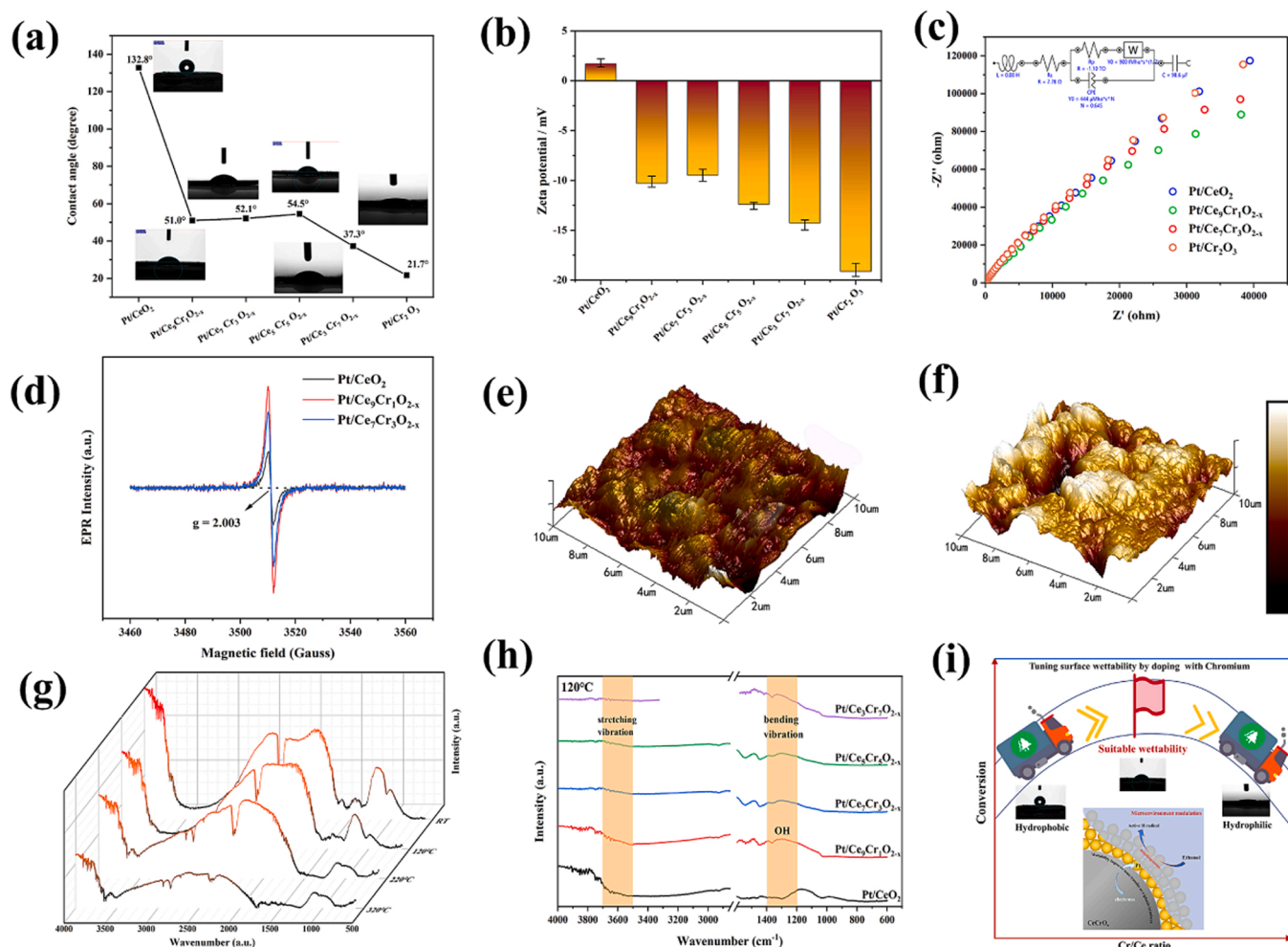


Fig. 9. (a) The contact angle of prepared materials. (b) Zeta potential values of catalysts. (c) Electrochemical impedance spectroscopy of the typical catalysts. (d) electron paramagnetic resonance (EPR) spectra. (e-f) the 10 $\mu\text{m} \times 10 \mu\text{m}$ 2D and 3D AFM images of Pt/CeO_2 and $\text{Pt/Ce}_9\text{Cr}_1\text{O}_{2-x}$. (g-h) in-situ FTIR spectra of $\text{Pt/Ce}_9\text{Cr}_1\text{O}_{2-x}$. (i) Structure-activity relationship between wettability and conversion.

hydrophilic nature of catalysts, which is favorable for mass transfer. The structure-activity relationship depicted in Fig. 9(i) demonstrates that the addition of appropriate Cr can significantly enhance the wettability of the catalyst. This improvement, in turn, enhances the mass transfer capacity at the triphasic interface, enabling direct transfer of reactants to the catalyst's active sites and accelerating the desorption of products, resulting in a significant improvement in catalytic activity [46].

The local coordination environment and metallic state of the active center on the supports play a crucial role in the hydrogenation reaction [47]. To identify the distribution and stability of the metal on the supports, H_2 -TPR experiments were conducted to analyze the interaction and redox properties of the as-synthesized catalysts. The results revealed that the Pt species in Pt/CeCrO_{2-x} can be entirely reduced under the conditions used in this work. As shown in Fig. 10a, the reduction peaks below 300 °C can be attributed to a two-step reduction of Pt^{4+} to Pt^{6+} and eventually to Pt^0 . The hydrogen consumption corresponding to each reduction peak of the catalyst is presented in Table S6. However, as the percentage of Cr in the sample increased, higher temperatures were required to reduce the metal, suggesting that Cr enhances the interaction between the metal and the support and can improve the stability of the catalyst. Upon partially magnified profile, each reduction profile was deconvoluted and divided into three reduction peaks approximately < 100 °C, 100–200 °C, and > 200 °C respectively. It is apparent that the reduction range of the $\text{Pt/Ce}_9\text{Cr}_1\text{O}_{2-x}$ catalyst is mainly distributed between 100 and 200 °C. This observation suggests that the surface

metals on $\text{Pt/Ce}_9\text{Cr}_1\text{O}_{2-x}$ are uniformly dispersed on the support, creating a similar chemical environment. In addition, $\text{Pt/Ce}_9\text{Cr}_1\text{O}_{2-x}$ catalyst has the highest concentration of oxygen vacancies (O_v). The density of O_v could be calculated by XPS, OSC, and Raman tests listed in Table S7. Raman spectra of the Pt/CeCrO_{2-x} catalyst with different Ce/Cr ratios was shown in Fig. S11. These results indicate that the interaction between Pt and CeCrO_{2-x} at the vacancy defects in support is critical for the stabilization of Pt NPs, which facilitates the charge transfer between Pt and support, resulting in enhanced hydrogenation performance [48].

In order to determine the metallic state of the active center on the supports, we utilized a Gaussian function to fit the asymmetric profiles and performed Pt 4f XPS spectra Fig. 10b. The results show that the Cr^{3+} doping resulted in the formation of more surface Pt^0 on the catalysts compared with the unmodified samples as evidenced by the integrated peak area. Specifically, Pt/CeCrO_{2-x} exhibited a negative shift of Pt 4f_{5/2} (74.8 eV) and Pt 4f_{7/2} (71.4 eV) compared to Pt/CeO_2 (74.6 and 71.2 eV, respectively). Conversely, the binding energy of Cr 2p and Ce 3d of $\text{Pt/Ce}_9\text{Cr}_1\text{O}_{2-x}$ showed positive shifts than that of Pt/CeO_2 (Figs. S4 and S10). These findings demonstrate that Pt anchored on the $\text{Ce}_9\text{Cr}_1\text{O}_2$ exhibits a positively charged state, while it approaches the metallic state on the CeO_2 [27,49]. In this work, Cr^{3+} acts as an electron donor to alter the electron density of the Pt on the surface in the form of an electron promoter. These shifts in binding energy can be attributed to electronic effects between the d orbitals of Pt, Cr, and Ce, resulting in

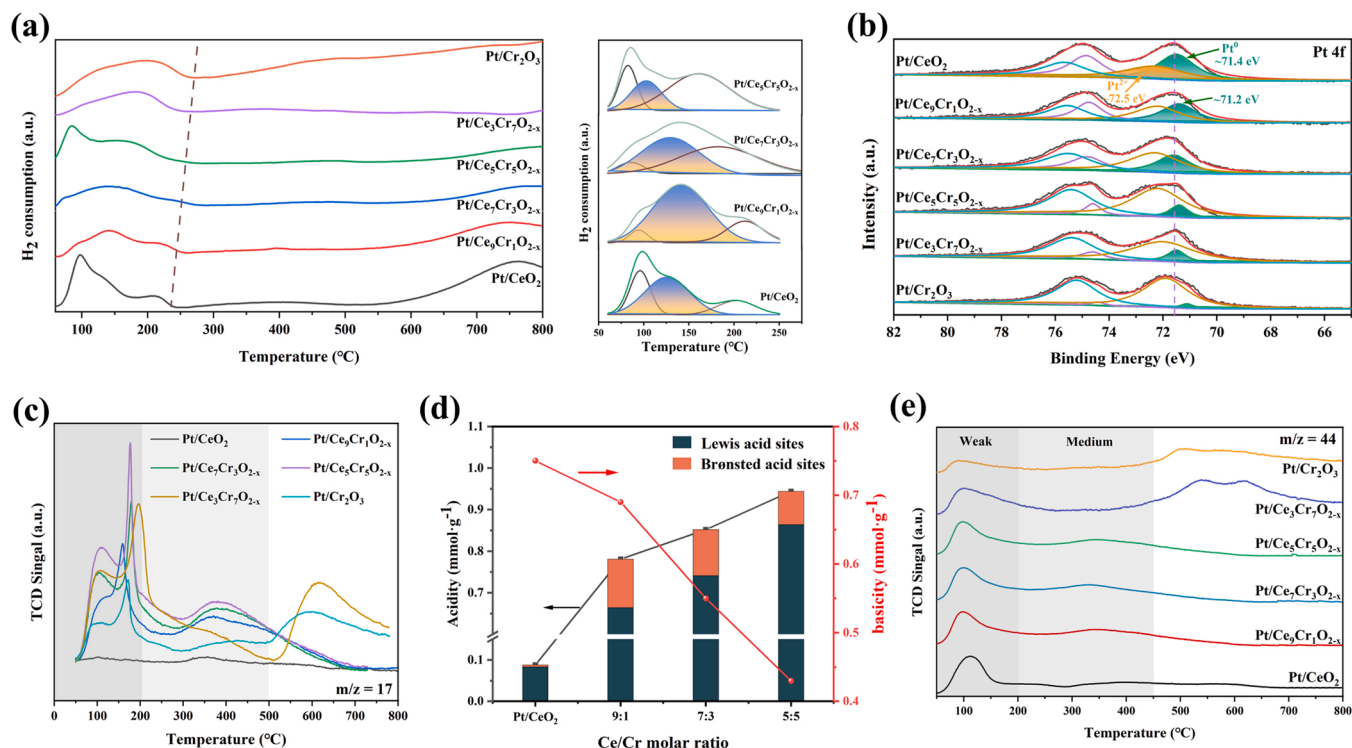
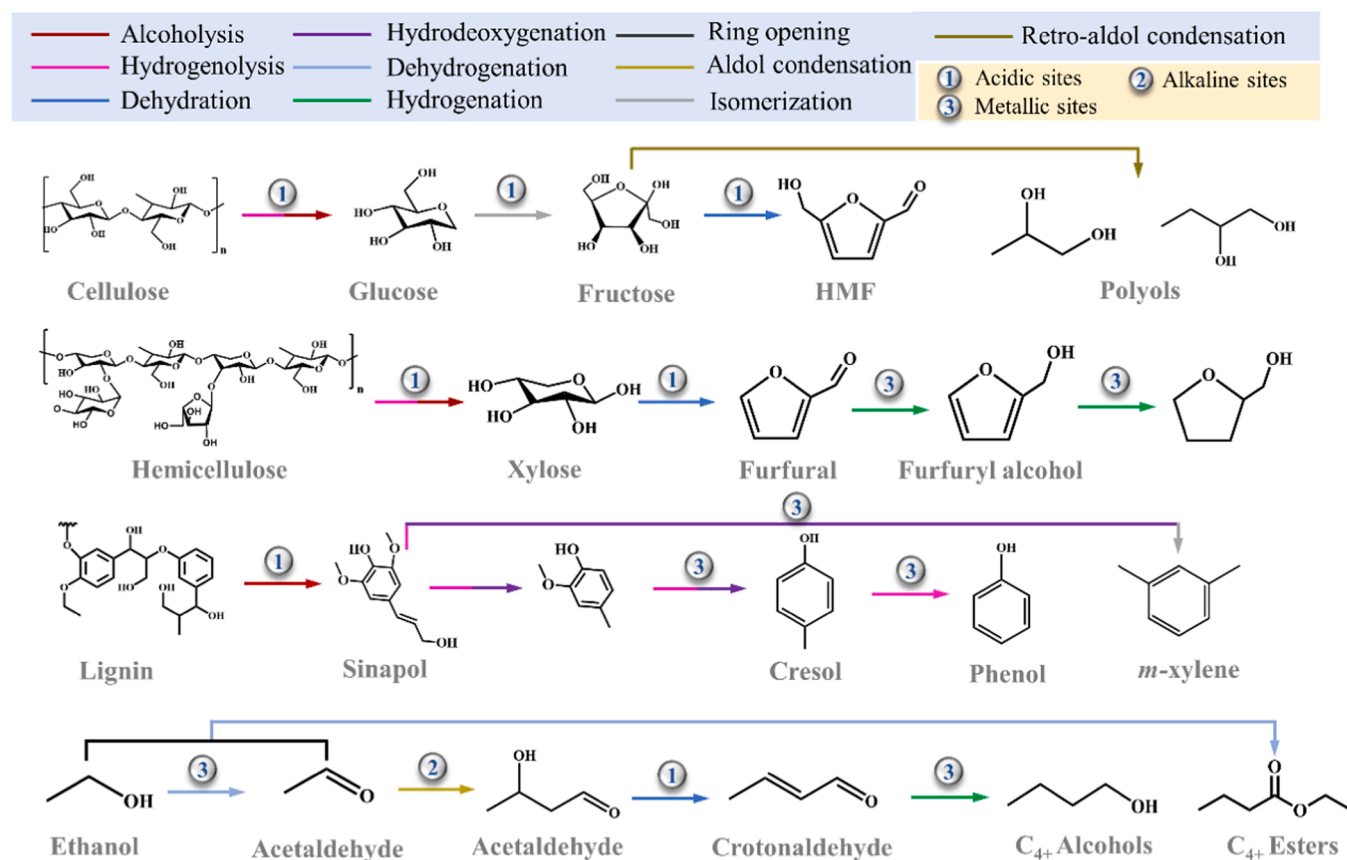


Fig. 10. (a) H₂-TPR and partially magnified profile. (b) XPS spectra of Pt 4f. (c) NH₃-TPD profiles. (d) The relationship between the acidity and alkalinity of the catalyst and the metal ratio. (e) CO₂-TPD profiles.



Scheme 1. Plausible reaction pathway for lignocellulose hydro-liquefaction in ethanol to obtain polyols and other fine chemicals.

electron transfer from support to Pt, which suggests a strong interaction between Pt and support [49].

What's more, ethanol dehydrogenation to acetaldehyde and Guerbet reaction is facilitated by both acid-base sites. To evaluate the acidity and basicity of the catalysts, NH_3 , CO_2 -TPD, and Py-DRIFT profiles were employed and the results are presented in Fig. 10(c-e). The NH_3 -TPD profiles were categorized into three regions: weak ($<250^\circ\text{C}$), medium ($250\text{--}400^\circ\text{C}$), and strong ($>400^\circ\text{C}$) [40]. The Pt/CeO_2 possesses negligible weak acid sites consistent with the assumption that CeO_2 is an alkaline metallic oxide. In contrast, which may be due to the addition of Cr, the modified catalysts showed higher acid density and acid intensity. Among them, $\text{Pt/Cr}_2\text{O}_3$ and $\text{Pt/Ce}_3\text{Cr}_7\text{O}_{2-x}$ have a more prominent number and density of acid sites. Its acidic sites in biomass hydro-liquefaction reactions, which activate C-O bonding and continuous dehydration, promote the hydrodeoxygenation process and thus improve product quality [8]. However, too many acidic sites on the catalyst can lead to undesired side reactions and increase the amount of residue and coke. Therefore, moderate acidic strength and concentration of $\text{Pt/Ce}_9\text{Cr}_1\text{O}_{2-x}$ catalysts are critical to achieve efficient conversion.

To explore the types and quantities of the surface acid sites, Py-DRIFT was employed. The results in Fig. 10d show that CeO_2 mainly provides Lewis acid sites and doping with a small amount of Cr can improve the acidity of the catalyst, especially Brønsted acid, and we speculate that CrO_x and Cr-OH-bridged hydroxyl groups promote the production of Brønsted acid sites based on literature and experimental data [50]. Previous studies have discussed the presence of a considerable amount of bridging surface hydroxyl groups that ultimately improve the surface energy and wettability of the catalyst. On the other hand, the alkalinity of the catalyst plays a key role in the carbon chain extension process. Usually, moderately strong bases are prone to aldol condensation. The CO_2 -TPD results are shown in Fig. 9e. The addition of small amounts of Cr does not seriously affect the alkalinity of the catalyst, and only when the Cr addition exceeds 70% of the catalyst, the alkali content and strength increase.

3.4. Plausible reaction paths

Based on the analysis of the products from the lignocellulose conversion and the characterization data, plausible reaction pathways are shown in Scheme 1. Under hydrothermal conditions, the glycosidic, ether, and ester linkage present in the three groups are cleaved through alcoholysis and hydrogenolysis [7,51]. The hydrogen radical utilized for hydrogenolysis is derived from the dehydrogenation reaction of ethanol. Then, some glucose fraction undergoes isomerization to fructose over Lewis acidic sites. Fructose and xylose dehydration over the acid sites produces their corresponding furanic aldehydes, namely, 5-Hydroxymethylfurfural (5-HMF) and furfural, respectively. In addition, fructose can undergo retro-aldol condensation to form erythrose and glycolaldehyde, which can be converted to ethylene glycol and other polyols. Lignin, a phenyl biopolymer consisting of three basic units, mainly produces phenol derivatives during HDO. The high content of aromatic rings in lignin makes these molecules highly resistant to degradation under high temperature and pressure conditions, making them ideal precursors for the formation of char. However, we did not observe a large amount of coke formation in this work. This can be attributed to the excellent hydrogen transfer efficiency that can quench radicals and unstable intermediate fragments, thus suppressing the formation of coke. This suppression of coke formation is achieved through a balance between the rate of depolymerization and stabilization.

4. Conclusions

In this study, we have successfully demonstrated a high-yield production of bio-oil and high-carbon alcohols from lignocellulose using $\text{Pt/Ce}_9\text{Cr}_1\text{O}_{2-x}$ catalyst in supercritical ethanol with minimal char formation. Pt and acid-based sites play a promotional role in promoting

reaction conversion, particularly those that involve H-transfers, such as ethanol dehydrogenation to acetaldehyde. The active hydrogen in ethanol can be transferred to the hydro-liquefaction reaction of biomass, and the aldol condensation of acetaldehyde generates higher carbon alcohol, which optimizes the quality of bio-oil and upgrades the ethanol solvent. Additionally, the isotope-labeled experiment demonstrated that the hydrogen derived from ethanol can participate in the hydrogenation reaction, thus, replacing the non-renewable hydrogen. Surface hydroxyl groups increased the hydrophilicity of the material, which was well dispersed in ethanol and facilitated contact with the substrates. CeCrO_{2-x} with strong oxophilicity and variable oxygen vacancies can serve as an excellent support for anchoring Pt nanoparticles and trapping reactants, resulting in an improved mass transfer capacity of the reaction. We believe that the integration of ethanol dehydrogenation and Guerbet reaction with biomass hydro-liquefaction will offer researchers a fresh approach to hydrogen transfer strategy, allowing for the complete utilization of endogenous hydrogen.

CRedit authorship contribution statement

Dong Liu and Bin Lou conceived and supervised the project. Weichao Chou and Pingping Lu synthesized the catalysts and performed catalytic experiments. Weizhen Li, Peng Wu, Zhuowu Men, and Chongchong Wu performed the material characterizations and analyzed the experimental results. Weichao Chou, Pingping Lu, and Bin Lou wrote the manuscript. Weizhen Li and Chongchong Wu supervised the project and reviewed the manuscript.

Declaration of Competing Interest

The authors declare no conflict of interest.

Data availability

Data will be made available on request.

Acknowledgments

The authors gratefully acknowledge financial support from the General project of National Natural Science Foundation of Shandong Province (ZR2023MB005), National Natural Science Foundation of China (22108309), Key Research and Development Project (Major Project of Scientific and Technological Innovation) of Shandong Province (2020CXGC010308), and the Taishan Scholar Program of Shandong (No. ts20190919).

Appendix A. Supporting information

Supplementary data associated with this article can be found in the online version at doi:10.1016/j.apcatb.2023.123320.

References

- [1] X. Si, R. Lu, Z. Zhao, X. Yang, F. Wang, H. Jiang, X. Luo, A. Wang, Z. Feng, J. Xu, Catalytic production of low-carbon footprint sustainable natural gas, *Nat. Commun.* 13 (2022) 1–9.
- [2] M. Antar, D. Lyu, M. Nazari, A. Shah, X. Zhou, D.L. Smith, Biomass for a sustainable bioeconomy: an overview of world biomass production and utilization, *Renew. Sustain. Energy Rev.* 139 (2021), 110691.
- [3] T. Stedile, L. Ender, H. Meier, E. Simionatto, V. Wiggers, Comparison between physical properties and chemical composition of bio-oils derived from lignocellulose and triglyceride sources, *Renew. Sustain. Energy Rev.* 50 (2015) 92–108.
- [4] L.R. Lynd, G.T. Beckham, A.M. Guss, L.N. Jayakody, E.M. Karp, C. Maranas, R. L. McCormick, D. Amador-Noguez, Y.J. Bomble, B.H. Davison, Toward low-cost biological and hybrid biological/catalytic conversion of cellulosic biomass to fuels, *Energy Environ. Sci.* 15 (2022) 938–990.
- [5] Z. Cao, M. Dierks, M.T. Clough, I.B.D. De Castro, R. Rinaldi, A convergent approach for a deep converting lignin-first biorefinery rendering high-energy-density drop-in fuels, *Joule* 2 (2018) 1118–1133.

- [6] Z. Sun, G. Bottari, A. Afanasenko, M.C. Stuart, P.J. Deuss, B. Fridrich, K. Barta, Complete lignocellulose conversion with integrated catalyst recycling yielding valuable aromatics and fuels, *Nat. Catal.* 1 (2018) 82–92.
- [7] S. Zhang, S.-F. Jiang, B.-C. Huang, X.-C. Shen, W.-J. Chen, T.-P. Zhou, H.-Y. Cheng, B.-H. Cheng, C.-Z. Wu, W.-W. Li, Sustainable production of value-added carbon nanomaterials from biomass pyrolysis, *Nat. Sustain.* 3 (2020) 753–760.
- [8] Z. Kaczor, Z. Buliński, S. Werle, Modelling approaches to waste biomass pyrolysis: a review, *Renew. Energy* 159 (2020) 427–443.
- [9] A. Akbarian, A. Andooz, E. Kowsari, S. Ramakrishna, S. Asgari, Z.A. Cheshmeh, Challenges and opportunities of lignocellulosic biomass gasification in the path of circular bioeconomy, *Bioresour. Technol.* (2022), 127774.
- [10] W. Chou, D. Liu, W. Li, X. Chou, H. Liu, C. Wu, P. Wu, Z. Men, Z. Li, Full utilization of lignocellulose through one-pot in-situ hydro-liquefaction with versatile Pt/CeCrO₂-x catalyst, *Appl. Catal. B Environ.* 316 (2022), 121625.
- [11] S. Nagappan, R.R. Bhosale, D.D. Nguyen, N.T.L. Chi, V.K. Ponnusamy, C.S. Woong, G. Kumar, Catalytic hydrothermal liquefaction of biomass into bio-oils and other value-added products—a review, *Fuel* 285 (2021), 119053.
- [12] C. Yuan, S. Wang, B. Cao, Y. Hu, A.E.-F. Abomohra, Q. Wang, L. Qian, L. Liu, X. Liu, Z. He, Optimization of hydrothermal co-liquefaction of seaweeds with lignocellulosic biomass: merging 2nd and 3rd generation feedstocks for enhanced bio-oil production, *Energy* 173 (2019) 413–422.
- [13] G.T. Jaya, R. Insyani, J. Park, A.F. Barus, M.G. Sibi, V. Ranaware, D. Verma, J. Kim, One-pot conversion of lignocellulosic biomass to ketones and aromatics over a multifunctional Cu–Ru/ZSM-5 catalyst, *Appl. Catal. B Environ.* 312 (2022), 121368.
- [14] X. Huang, C. Atay, T.I. Korányi, M.D. Boot, E.J. Hensen, Role of Cu–Mg–Al mixed oxide catalysts in lignin depolymerization in supercritical ethanol, *ACS Catal.* 5 (2015) 7359–7370.
- [15] X. Wu, X. Fan, S. Xie, J. Lin, J. Cheng, Q. Zhang, L. Chen, Y. Wang, Solar energy-driven lignin-first approach to full utilization of lignocellulosic biomass under mild conditions, *Nat. Catal.* 1 (2018) 772–780.
- [16] Q. Xia, Z. Chen, Y. Shao, X. Gong, H. Wang, X. Liu, S.F. Parker, X. Han, S. Yang, Y. Wang, Direct hydrodeoxygenation of raw woody biomass into liquid alkanes, *Nat. Commun.* 7 (1) (2016) 10.
- [17] C.P. Jiménez-Gómez, J.A. Cecilia, I. Márquez-Rodríguez, R. Moreno-Tost, J. Santamaría-González, J. Mérida-Robles, P. Mairesles-Torres, Gas-phase hydrogenation of furfural over Cu/CeO₂ catalysts, *Catal. Today* 279 (2017) 327–338.
- [18] N. Hao, K. Alper, K. Tekin, S. Karagoz, A.J. Ragauskas, One-pot transformation of lignocellulosic biomass into crude bio-oil with metal chlorides via hydrothermal and supercritical ethanol processing, *Bioresour. Technol.* 288 (2019), 121500.
- [19] K.M. Isa, T.A.T. Abdullah, U.F.M. Ali, Hydrogen donor solvents in liquefaction of biomass: a review, *Renew. Sustain. Energy Rev.* 81 (2018) 1259–1268.
- [20] P. Sudarsanam, R. Zhong, S. Van den Bosch, S.M. Coman, V.I. Parvulescu, B.F. Sels, Functionalised heterogeneous catalysts for sustainable biomass valorisation, *Chem. Soc. Rev.* 47 (2018) 8349–8402.
- [21] A. Chacon-Parra, D. Lewis, P. van Eyk, Elemental nitrogen balance, reaction kinetics and the effect of ethanol on the hydrothermal liquefaction of soy protein, *Chem. Eng. J.* 425 (2021), 130576.
- [22] X. Huang, T.I. Korányi, M.D. Boot, E.J. Hensen, Catalytic depolymerization of lignin in supercritical ethanol, *ChemSusChem* 7 (2014) 2276–2288.
- [23] X. Huang, T.I. Korányi, M.D. Boot, E.J. Hensen, Ethanol as capping agent and formaldehyde scavenger for efficient depolymerization of lignin to aromatics, *Green Chem.* 17 (2015) 4941–4950.
- [24] A.D. Liyanage, S.D. Perera, K. Tan, Y. Chabal, K.J. Balkus Jr, Synthesis, characterization, and photocatalytic activity of Y-doped CeO₂ nanorods, *ACS Catal.* 4 (2014) 577–584.
- [25] X. Xu, L. Liu, Y. Tong, X. Fang, J. Xu, D.-e. Jiang, X. Wang, Facile Cr³⁺-doping strategy dramatically promoting Ru/CeO₂ for low-temperature CO₂ methanation: unraveling the roles of surface oxygen vacancies and hydroxyl groups, *ACS Catal.* 11 (2021) 5762–5775.
- [26] M.A. Goldberg, A.V. Akopyan, M.R. Gafurov, O.N. Makshakova, N.O. Donskaya, A. S. Fomin, P.P. Polikarpova, A.V. Anisimov, F.F. Murzakhanov, A.V. Leonov, Iron-doped mesoporous powders of hydroxyapatite as molybdenum-impregnated catalysts for deep oxidative desulfurization of model fuel: synthesis and experimental and theoretical studies, *J. Phys. Chem. C* 125 (2021) 11604–11619.
- [27] P.L. Kress, S. Zhang, Y. Wang, V. Çınar, C.M. Friend, E.C.H. Sykes, M. Montemore, A priori design of dual-atom alloy sites and experimental demonstration of ethanol dehydrogenation and dehydration on PtCrAg, *J. Am. Chem. Soc.* 145 (2023) 8401–8407.
- [28] N.-C. Lai, G. Cong, Z. Liang, Y.-C. Lu, A highly active oxygen evolution catalyst for lithium-oxygen batteries enabled by high-surface-energy facets, *Joule* 2 (2018) 1511–1521.
- [29] B.G. Reed-Berendt, D.E. Latham, M.B. Dambatta, L.C. Morrill, Borrowing hydrogen for organic synthesis, *ACS Cent. Sci.* 7 (2021) 570–585.
- [30] H. Aitchison, R.L. Wingad, D.F. Wass, Homogeneous ethanol to butanol catalysis□ Guerbet renewed, *ACS Catal.* 6 (2016) 7125–7132.
- [31] S. Yamaguchi, M. Yabushita, M. Kim, J. Hirayama, K. Motokura, A. Fukuoka, K. Nakajima, Catalytic conversion of biomass-derived carbohydrates to methyl lactate by acid–base bifunctional γ -Al₂O₃, *ACS Sustain. Chem. Eng.* 6 (2018) 8113–8117.
- [32] B. Biswas, A. Kumar, R. Kaur, B.B. Krishna, T. Bhaskar, Catalytic hydrothermal liquefaction of alkali lignin over activated bio-char supported bimetallic catalyst, *Bioresour. Technol.* 337 (2021), 125439.
- [33] Z.D. Young, R.J. Davis, Hydrogen transfer reactions relevant to Guerbet coupling of alcohols over hydroxyapatite and magnesium oxide catalysts, *Catal. Sci. Technol.* 8 (2018) 1722–1729.
- [34] S. Hanspal, Z.D. Young, H. Shou, R.J. Davis, Multiproduct steady-state isotopic transient kinetic analysis of the ethanol coupling reaction over hydroxyapatite and magnesia, *ACS Catal.* 5 (2015) 1737–1746.
- [35] S. Crowley, M.J. Castaldi, Mechanistic insights into catalytic ethanol steam reforming using isotope-labeled reactants, *Angew. Chem.* 128 (2016) 10808–10813.
- [36] P. Yan, E. Kennedy, M. Stockenhuber, Natural zeolite supported Ni catalysts for hydrodeoxygenation of anisole, *Green Chem.* 23 (2021) 4673–4684.
- [37] J. Yu, W. Chen, K. Li, C. Zhang, M. Li, F. He, L. Jiang, Y. Li, W. Song, C. Cao, Graphdiyne nanospheres as a wettability and electron modifier for enhanced hydrogenation catalysis, *Angew. Chem.* 134 (2022), e202207255.
- [38] Y. Qiu, C. Wu, I.D. Gates, Y. Yang, S. Guo, Z. Men, B. Lou, X. Yang, N. Shi, F. Wen, Isolated Co-Ti-Y trimetallic synergistic catalysis based on apparent anti-electronegative polarization, *Adv. Funct. Mater.* 32 (2022), 2207482.
- [39] K. Gurushantha, K. Anantharaju, S. Sharma, H. Nagaswarupa, S. Prashantha, K. V. Mahesh, L. Renuka, Y. Vidya, H. Nagabhushana, Bio-mediated Sm doped nano cubic zirconia: photoluminescent, Judd–Ofelt analysis, electrochemical impedance spectroscopy and photocatalytic performance, *J. Alloy. Compd.* 685 (2016) 761–773.
- [40] Y. Qiu, B. Lou, X. Yang, Y. Fu, N. Shi, C. Yin, F. Wen, Y. Zhang, X. Yin, L. Wu, Toward understanding the manipulation of surface acidity behavior with relativistic effect for the formation of C–N bonds, *ACS Appl. Eng. Mater.* 1 (2022) 436–446.
- [41] C. Cupak, P. Szabo, H. Biber, R. Stadlmayr, C. Grave, M. Fellinger, J. Brötzner, R. Wilhelm, W. Möller, A. Mutzke, Sputter yields of rough surfaces: Importance of the mean surface inclination angle from nano-to microscopic rough regimes, *Appl. Surf. Sci.* 570 (2021), 151204.
- [42] S.H. Park, S.Y. Byeon, J.-H. Park, C. Kim, Insight into the critical role of surface hydrophilicity for dendrite-free zinc metal anodes, *ACS Energy Lett.* 6 (2021) 3078–3085.
- [43] A. Kordijazi, S.K. Behera, S. Suri, Z. Wang, M. Povolito, N. Salowitz, P. Rohatgi, Data-driven modeling of wetting angle and corrosion resistance of hypereutectic cast aluminum-silicon alloys based on physical and chemical properties of surface, *Surf. Interfaces* 20 (2020), 100549.
- [44] A. Ali, C. Zhao, Ru nanoparticles supported on hydrophilic mesoporous carbon catalyzed low-temperature hydrodeoxygenation of microalgae oil to alkanes at aqueous-phase, *Chin. J. Catal.* 41 (2020) 1174–1185.
- [45] X. Guo, B. Liu, X. Gao, F. He, Q. Ma, S. Fan, T.-s. Zhao, J. Tian, P. Reubroycharoen, J. Zhang, Improved olefin selectivity during CO hydrogenation on hydrophilic Fe/HAP catalysts, *Catal. Today* 410 (2023) 193–204.
- [46] Z. Li, R. Hu, J. Song, L. Liu, J. Qu, W. Song, C. Cao, Gas–liquid–solid triphase interfacial chemical reactions associated with gas wettability, *Adv. Mater. Interfaces* 8 (2021), 2001636.
- [47] W. Chou, P. Wu, M. Luo, W. Li, S. Li, Effects of Al, Si, Ti, Zr promoters on catalytic performance of iron-based Fischer–Tropsch synthesis catalysts, *Catal. Lett.* 150 (2020) 1993–2002.
- [48] Z. Kong, Y. Li, Y. Wang, Y. Zhang, K. Shen, X. Chu, H. Wang, J. Wang, L. Zhan, Monodispersed MnOx–CeO₂ solid solution as superior electrocatalyst for Li₂S precipitation and conversion, *Chem. Eng. J.* 392 (2020), 123697.
- [49] Y.-Y. Feng, H.-S. Hu, G.-H. Song, S. Si, R.-J. Liu, D.-N. Peng, D.-S. Kong, Promotion effects of CeO₂ with different morphologies to Pt catalyst toward methanol electrooxidation reaction, *J. Alloy. Compd.* 798 (2019) 706–713.
- [50] A. García, P.J. Miguel, A. Ventimiglia, N. Dimitratos, B. Solsona, Optimization of the Zr-loading on siliceous support catalysts leads to a suitable Lewis/Brønsted acid sites ratio to produce high yields to γ -valerolactone from furfural in one-pot, *Fuel* 324 (2022), 124549.
- [51] Y. Jing, Y. Guo, Q. Xia, X. Liu, Y. Wang, Catalytic production of value-added chemicals and liquid fuels from lignocellulosic biomass, *Chem* 5 (2019) 2520–2546.